

Simulations of X-rays from Solar Wind Charge Exchange at Mars: Parameter dependence

H. Gunell* and M. Holmström

Swedish Institute of Space Physics, Box 812, SE-981 28 Kiruna, Sweden

E. Kallio and P. Janhunen

Finnish Meteorological Institute, Helsinki, Finland

K. Dennerl

Max-Planck-Institut für extraterrestrische Physik, Garching, Germany

(Dated: Received 2 December 2004; received in revised form 23 May 2005; accepted 14 June 2005)

A hybrid simulation of the solar wind-Mars interaction and a test particle simulation of heavy ion trajectories near Mars are used to compute the contribution from solar wind charge exchange processes to the X-ray emission from Mars. Here we study how the simulated X-ray emissions depend on the parameters of the simulation model. Solar wind parameters are estimated using a ballistic model based on data from the WIND satellite and using an MHD model that uses inputs from interplanetary scintillation measurements. These two models produce X-ray images with significantly different structure. The intensity of the X-ray emissions and the size of the X-ray halo are also found to increase with an increasing exobase neutral temperature.

Keywords: Solar wind-Mars interaction, X-ray, Solar wind charge exchange, Hybrid simulation

I. INTRODUCTION

Observations of planetary X-ray emissions have been made in recent years. X-rays from Venus (Dennerl et al., 2002) and Mars (Dennerl, 2002) were discovered using the Chandra X-ray observatory.

A disk the size of Mars dominated by fluorescent scattering of solar X-rays was found when Mars was observed in the year 2001. Around the disk a faint X-ray halo was detected. It cannot be explained by fluorescence, since the fluorescence peak, that is seen in the emissions from the disk, is absent in the X-ray emissions from the halo (Dennerl, 2002), and fluorescence is an efficient process only at low altitudes. Dennerl (2002) suggested that the halo could be caused by the solar wind charge exchange (SWCX) process. Gunell et al. (2004) performed a computer simulation that showed that charge exchange processes are consistent with the observations of the Martian X-ray halo.

Fluorescence occurs when X-rays emitted by the sun are absorbed by neutrals in the planetary atmosphere, and then re-emitted isotropically. Elastic scattering of solar X-rays can also occur in planetary atmospheres. A detailed, analysis of the intensity of the X-rays produced by these two mechanisms was done by Cravens and Mau-

rellis (2001).

X-rays are emitted through the solar wind charge exchange process wherever the solar wind meets a neutral atmosphere. A small fraction of the solar wind consists of heavy, multiply charged ions such as O^{6+} , C^{6+} , and Ne^{8+} . Charge-exchange collisions between these ions and neutral atoms can leave the ions in highly excited states. When the thus captured electrons transit to lower energy states, photons in the soft X-ray range may be emitted. Cravens (1997) first proposed this process as an explanation for the observations of X-rays from comets, and it is likely the dominant process for generation of cometary X-rays (Cravens, 2002). SWCX has also been suggested as a mechanism for generation of X-rays at Mars (Cravens, 2000; Krasnopolsky, 2000). Computer simulations of the intensities and morphology of these emissions were presented by Holmström et al. (2001) for Mars.

In a previous paper (Gunell et al., 2004) we conducted simulations of a large number of heavy solar wind species: O^{7+} , C^{6+} , O^{6+} , O^{8+} , Mg^{10+} , Mg^{9+} , Si^{9+} , N^{6+} , C^{5+} , Ne^{8+} , Fe^{9+} , S^{9+} , Si^{8+} , Fe^{11+} , and Mg^{8+} . The simulation results were compared to observations made by Dennerl (2002). In this work we investigate how changes in the different parameters of the simulation model influence the X-ray emissions by comparing the results of simulations with different parameters for two ion species, namely O^{7+} and C^{6+} . In both the present and the previous paper a quasi-neutral hybrid model is used to obtain estimates of the electric and magnetic fields in the vicinity of Mars, and the heavy ion trajectories are computed using those fields. Two sets of solar wind parameters

*also at: Space Technology Ireland, National University of Ireland, Maynooth, Co. Kildare, Ireland; Electronic address: herbert.gunell@physics.org

are compared: one estimate obtained using a ballistic model based on data obtained by the WIND satellite near the Earth; and another estimate that results from MHD tomography based on interplanetary scintillation (IPS) data. The influence of changes in the neutral exosphere is also studied by varying the exobase temperature.

The paper is organised as follows. In section II the simulation model is described, and in section III the results of the different solar wind parameter estimates are presented. In section IV the influence of the exobase temperature is studied, in section V the heavy ion abundances are discussed, and in section VI conclusions are presented and discussed.

II. SIMULATION MODEL

Here we present the method by which we have produced simulated images of SWCX at Mars that corresponds to the observation by Dennerl (2002).

The calculations were performed in three steps. First the solar wind parameters were estimated using two different models: one ballistic model based on data obtained by the WIND spacecraft and one MHD tomographic model using inputs from IPS measurements. The second step was to run a hybrid simulation of the interaction of the solar wind with Mars using the input parameters obtained in step one. The third and final step was to run a test particle simulation, calculating the trajectories of heavy solar wind ions in the electric and magnetic fields obtained in step two. That the heavy ions are not modelled self consistently can be justified since they only constitute a small fraction of the solar wind. Then using models for the neutral exosphere densities and the charge exchange cross sections the X-ray emissions from Mars could be obtained.

A. Parameter estimation

Since Mars was near opposition the plasma that was sampled by WIND near the Earth on July 2, 2001 arrived at Mars two days later during the X-ray observation. The solar wind data were scaled with the distance from the sun, and the average parameter values over the period of the observation were used as input parameters for a hybrid simulation. These parameters are shown in the left column of table I. The parameter estimation process is illustrated in Fig. 1. Fig. 1(a) shows the relative positions of the sun, Mars, and Earth. Fig. 1(b) was calculated from the v_x data and shows how the arrival time at Mars of a particular plasma element depends on the time it passed by the Earth. The horizontal dashed lines mark the beginning and end of the X-ray observation, and the vertical dashed lines show the beginning and end of the time interval that is used to compute the average parameters shown in table I. Panels (c-h) of Fig. 1 show these

parameters at Earth as measured during the interval that is marked by the vertical lines in Fig. 1(b).

The parameters are estimated in the following way. The arrival time at Mars of a particular plasma element as a function of the time it passed by the Earth was calculated from the v_x data. This gives an interval, starting at 00:57:49 (UT) and ending 18:49:49 (UT) on July 2, over which the plasma parameters are averaged. The plasma that passed the Earth during this interval reached Mars during the observation two days later. We use a Mars-centred coordinate system with the sun in the positive x -direction, a northerly z -axis that is perpendicular to the ecliptic, and a y -direction that closes the right-handed system. The solar wind speed v_{sw} and the proton temperature $T_{p,sw}$ are assumed to be constants, and are simply the average values of v_x and T_p . The density n_{sw} is scaled by the squared ratio of the two planets respective distances from the sun: $n_{sw} = n_p/1.446^2$. The z -component of the magnetic field is smaller than the other two for most of the observation, and therefore $B_z = 0$ is assumed. We have assumed that the direction of the magnetic field is given by a Parker-spiral, which means that B_y/B_x is proportional to the distance from the sun. Thus the magnetic field is $\vec{B}_{sw} = (B_x/1.446^2, B_y/1.446, 0)$.

The parameters shown in the right column of table I were estimated using MHD tomography based on IPS measurements (Hayashi et al., 2003). The Solar-Terrestrial Environment Laboratory (STEL) at Nagoya University measures the radio flux from distant radio sources at four sites. The processed result is the solar wind velocity averaged along lines of sight. To resolve the solar wind parameters at a particular point they use an MHD code to model the evolution of the solar wind outside a sun-centred sphere with a radius of 50 solar radii. Remote sensing of the photospheric magnetic field is used for the magnetic boundary conditions at 50 solar radii, and analytical fits to Helios data are used for the density boundary conditions. The boundary conditions are discussed further by Hayashi et al. (2003).

B. Hybrid simulation

The second step was running a hybrid simulation of the interaction between the solar wind and Mars (Kallio and Janhunen, 2001, 2002) to obtain the electric and magnetic fields around Mars at the time of the observation. The hybrid code was run using 1.7×10^6 particles, with a fully absorbing obstacle boundary at $R_{\text{obst}} = 3600$ km. The simulation box was a Mars-centred $6R_{\text{obst}} \times 6R_{\text{obst}} \times 6R_{\text{obst}}$ cube. A grid with three different cell sizes, namely $0.05R_{\text{obst}}$, $0.1R_{\text{obst}}$, and $0.2R_{\text{obst}}$, was used. The smallest cells were used close to the planet on the dayside.

TABLE I Average solar wind parameters at Mars on July 4, 2001, 11:47–21:00 (UT) as estimated from WIND data (left column), and through MHD tomography of IPS data (right column).

	WIND	IPS
v_{sw}	330 km/s	434 km/s
n_{sw}	$4.40 \times 10^6 \text{ m}^{-3}$	$2.63 \times 10^6 \text{ m}^{-3}$
$T_{p,sw}$	$4.56 \times 10^4 \text{ K}$	$5.61 \times 10^4 \text{ K}$
\vec{B}	$(1.38, -4.43, 0) \text{ nT} =$ $4.64 \text{ nT} \cdot (\cos(72.7^\circ), -\sin(72.7^\circ), 0)$	$(0.639, -0.915, 9.63 \times 10^{-4}) \text{ nT} =$ $1.12 \text{ nT} \cdot (\cos(55^\circ), -\sin(55^\circ), 0)$

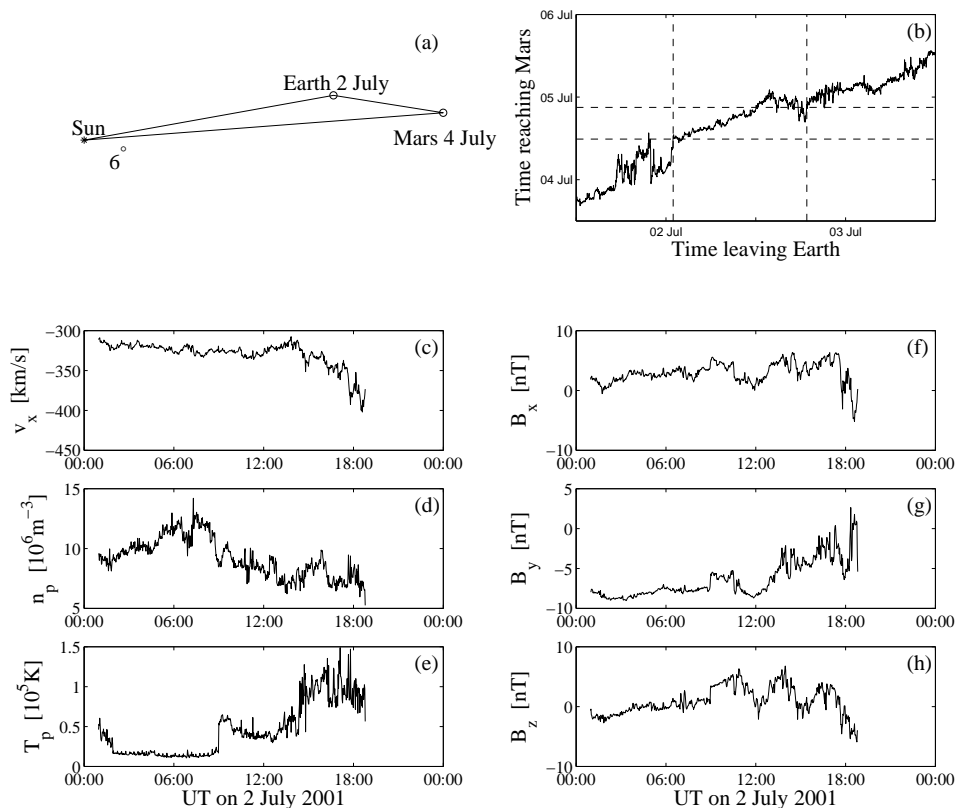


FIG. 1 (a) The positions of Mars and Earth relative to the sun. (b) The arrival time at Mars of solar wind plasma elements as a function of the time they passed by the Earth. The horizontal dashed lines mark the interval of the X-ray observation, i.e., from 11:47:39 (UT) and 21:00:30 (UT) on July 4, 2001, and the vertical dashed lines mark the interval that the plasma that arrived at Mars during the X-ray observation left the Earth. (c) v_x , (d) n_p , (e) T_p , (f) B_x , (g) B_y , and (h) B_z between 00:57:49 and 18:49:49 on July 2, 2001, i.e., the interval marked by vertical dashed lines in panel (b).

C. Test particle simulation

The third step was to run a test particle simulation, calculating the trajectories of heavy solar wind ions in the electric and magnetic fields that were obtained from the hybrid simulation, and for each time step of the test particle simulation saving the X-ray emission density on a grid. The trajectories were computed by integrating the Lorentz force using Boris' CYLRAD algorithm (see for example Hockney and Eastwood (1988)) One hundred thousand trajectories were calculated for each of the ion

species O^{7+} and C^{6+} . These species were selected from table 1 of Schwadron and Cravens (2000) for being the ion species that generate the highest luminosity, and together comprising 47 % of the total luminosity of the species of in that table. In our previous paper (Gunell et al., 2004) the calculations were performed for a large number of ion species. In this work we concentrate on the two species that generate the highest luminosity, and study the effects of changes in the parameters of the solar wind and the exosphere. The test particles were injected in the simulation box of the hybrid simulation at its upstream

TABLE II Exobase densities and temperatures for the neutral species that are included in the exosphere model.

Species	Density	Temperature
H	$3.1 \times 10^{10} \text{ m}^{-3}$	0.31 kK
H ₂	$4.3 \times 10^{11} \text{ m}^{-3}$	0.37 kK
<i>O_{thermal}</i>	$3.3 \times 10^{14} \text{ m}^{-3}$	0.38 kK
<i>O_{hot}</i>	$3.1 \times 10^{10} \text{ m}^{-3}$	4.6 kK

edge. The initial velocity distribution was assumed to be a Maxwellian with temperature $T_{p,sw}$ that is centred around the drift speed v_{sw} . In our previous paper we assumed that all species have the same temperature and that this temperature is equal to the temperature of the solar wind protons. Hefti et al. (1998) showed that both cases where the temperatures of the protons and heavy ions are equal and cases where their thermal speeds are equal occur in the solar wind. The trend towards equal temperature diminishes with increasing m/q^2 , i.e., the ratio of mass to charge squared. For O^{7+} and C^{6+} , the species studied here, $m/q^2 \approx 0.3$, and both the case with equal temperatures and that with equal thermal speeds could occur. In this work we have chosen to study the more likely equal thermal speeds case.

The cross sections for charge exchange (σ), the relative abundance of each ion species in the solar wind (a), and the energy released ($E_{n \rightarrow n_0}$) were taken from table 1 of Schwadron and Cravens (2000). The cross sections reported by Schwadron and Cravens (2000) are for charge exchange collisions between heavy ions and water molecules, but since the ionisation potentials for O, H, and H₂ are close to that of water using the cross sections for water is a reasonable approximation (Wegmann et al., 1998). An excited ion may go through several intermediate states before reaching the ground state, and thus release its energy to several photons. We use a simplified model, assuming that the transition to the ground state occurs in either one or two steps (Schwadron and Cravens, 2000; Wegmann et al., 1998). The neutral exosphere was modelled using a Chamberlain exosphere (Chamberlain and Hunten, 1987), which is a spherically symmetric model. The model included atomic hydrogen, molecular hydrogen, and one hot and one thermal population of atomic oxygen. Exobase densities for solar maximum conditions (Kallio et al., 1997; Krasnopolsky and Gladstone, 1996) were used for these species. The exobase altitude is 170 km. The exobase densities and temperatures are shown in table II. The exobase conditions (temperature and density) have large temporal and spatial variations (Keating et al., 1998), resulting in large variations of exospheric densities. In section IV the exobase temperature is varied by multiplying the temperatures in table II by 0.2; 0.5; 1; 2; and 5.

The mathematical formulation below follows Gunell et al. (2004) with small changes of the notation. Each test

particle represents a large number of solar wind ions, and this number decreases as the test particle moves through the simulation area, where some of the real particles it represents are lost in charge exchange collisions. The density n_i represented by the test particle “i” is

$$n_i(s) = n_{sw} a_\alpha e^{-\sigma_\alpha \int_0^s N(s') ds'} \quad (1)$$

where n_{sw} is the solar wind proton density, s the path length along the trajectory, $N(s) = N_{\text{O}}(s) + N_{\text{H}}(s) + N_{\text{H}_2}(s)$ the density of the neutral exosphere, and a_α is the relative abundance of the particular ion species α in the solar wind, i.e., $a_\alpha = n_i(0)/n_{sw}$. σ_α is the cross section for charge exchange collisions between the ion species α to which the test particle “i” belongs and the neutral gas. The contribution from one test particle “i” to the density of the emitted X-ray power is then

$$\begin{aligned} P_i(s) &= -\frac{dn_i}{dt} E_{n \rightarrow n_0} \\ &= n_{sw} a_\alpha \sigma_\alpha N(s) v_i(s) e^{-\sigma_\alpha \int_0^s N(s') ds'} E_{n \rightarrow n_0} \end{aligned} \quad (2)$$

For each test particle “i” at each time step the quantity

$$\Lambda_i = N(s) v_i(s) e^{-\sigma_\alpha \int_0^s N(s') ds'} \frac{\Delta t}{\Delta x \Delta y \Delta z} \quad (3)$$

is accumulated on a grid, in a way that is analogous with the way charge is assigned to a grid in a particle in cell simulation. In equation (3) $\Delta t = 0.25$ s is the time step and $\Delta x \Delta y \Delta z$ is the volume of a grid element. We have used $\Delta x = \Delta y = \Delta z = 3.5 \times 10^5$ m. The total emitted X-ray power density is then found by summation of the contributions from all ion species.

Ions can, in principle, undergo several charge exchange collisions until they have lost all their charge, emitting photons in each step. This means that O^{7+} ions after a charge exchange collisions are a source of O^{6+} ions. We have neglected this source term after examining the exponential function $\exp(-\sigma_\alpha \int_0^s N(s') ds')$ of Eq. (1). The value of the exponential when a test particle leaves the system, either by precipitating on the atmosphere or by leaving through the outer boundary of the simulation box, is a measure of what fraction of the original density still remains. If the value of the exponential is still close to unity when the particles leave the system the traversed region of the atmosphere can be considered collisionally thin and the additional source term is negligible. The average value of this factor computed using ten thousand test particles of the most important species, i.e., O^{7+} and C^{6+} , is 0.85 and 0.92 respectively. We thus find it justified to neglect this small ion source.

The X-ray flux $p(\xi, \zeta)$ that can be observed by an observer at Earth is found by integration along lines of sight. Since the observer is very far away we use a parallel projection.

$$p(\xi, \zeta) = \frac{1}{4\pi} \int \sum_i P_i(x, y, z) ds \quad (4)$$

is the directional X-ray energy flux measured in watts per square metre and steradian. The summation over the index i is a summation over all test particles of all ion species. ξ corresponds to the offset along the solar direction in the ecliptic plane and the elevation angle ζ to the offset perpendicular to the solar direction, both perpendicular to the line of sight. Simulated X-ray images such as those shown in Fig. 2 show the directional X-ray energy flux from Mars. In each image the inner white circle, with radius 10.2 arc seconds, marks the geometric size of Mars, and the outer white circle, with radius 30 arc seconds marks the extent of the X-ray halo according to Dennerl (2002). The grey-scale shows the X-ray radiance in $\text{Wm}^{-2}\text{sr}^{-1}$. In Fig. 2 we have included only photons with energies above 200 eV. The photon energy is modelled, following Schwadron and Cravens (2000), under the assumption that an ion in its excited state (quantum number n) emits its energy, $E_{n \rightarrow n_0}$, in either one or two steps, and that all transitions have an equal probability given by $1/(n - n_0)$. The X-ray flux shown in the images is thus

$$p_E(\xi, \zeta) = \frac{Sv_{sw}n_{sw}}{4\pi} \sum_{\alpha} \frac{a_{\alpha}\sigma_{\alpha}}{N_{tp,\alpha}} \int \Lambda_{\alpha} ds \sum_{E_{ph} > E} \frac{E_{ph}}{n - n_0} \quad (5)$$

where S is the cross section of the simulation box, i.e. the area across which test particles are uniformly injected, $N_{tp,\alpha}$ is the number of test particles for ion species α , E_{ph} is the photon energy, and $E = 200$ eV is the minimum energy of the photons included in the image. For $E = 0$, that is, if all photons were included, $p_E(\xi, \zeta) = p(\xi, \zeta)$. The photon energies E_{ph} and the quantum numbers n and n_0 are species dependent even though the species index α has been dropped.

$$\Lambda_{\alpha} = \sum_i \Lambda_i$$

where the sum is taken over all test particles “ i ” of ion species α .

To be able to compare with observations the energy dependent effective detector area $A(E_{ph})$ has to be taken into account. The observed directional flux expressed as a count rate, measured in units of $\text{s}^{-1}\text{sr}^{-1}$, is

$$c_{AE}(\xi, \zeta) = \frac{Sv_{sw}n_{sw}}{4\pi} \sum_{\alpha} \frac{a_{\alpha}\sigma_{\alpha}}{N_{tp,\alpha}} \int \Lambda_{\alpha} ds \sum_{E_{ph} > E} \frac{A(E_{ph})}{n - n_0} \quad (6)$$

The radial distribution of the X-ray power is obtained by changing to polar coordinates and integrating over the azimuthal angle. This is shown in Fig. 3, where the thin solid curve displays the quantity

$$f(\rho) = \frac{1}{2\pi} \int_0^{2\pi} c_{AE}(\rho, \varphi) d\varphi \quad (7)$$

where ρ is the radial and φ is the azimuthal polar coordinate of Fig. 2.

III. COMPARISON OF THE INFLUENCE OF DIFFERENT SOLAR WIND PARAMETERS

The hybrid code was run twice using two different sets of input parameters, that were estimated as described in section II.A. The parameters are shown in table I. The simulated X-ray images based on these two different sets of input data are shown in Fig. 2. The maximum radiance in the image based on the IPS parameters is higher than that in the image that is based on WIND parameters by approximately a factor of two. There is also a noticeable asymmetry in the IPS image, which has most of the emissions at the lower right hand side of the image centre.

The radial distribution of the X-ray power obtained from Eq. (7) is shown in Fig. 3 for the simulation that is based on WIND parameters (solid line) and IPS parameters (dashed line). It is seen in the figure that the X-ray emissions from the outer halo are similar in the two cases. Close to the planet, however, the IPS parameters result in higher emission. This is true for the inner halo ($10.2'' \leq \rho \leq 14.2''$) and for the disk of Mars ($\rho \leq 10.2''$). The differences for the inner halo indicate that the WIND parameters agree better with the observations of the X-ray halo, c.f., Gunell et al. (2004). To make a more detailed comparison with data the computations should be performed for the whole list of solar wind ion species, and the computational results should preferably be compared to observations with better photon statistics.

In Fig. 4 the X-ray emission region is shown in a cylindrical system of coordinates. One can again see that the emissions are stronger in simulation using IPS parameters, and that this difference in emission rates is largest at low altitudes. The structure of the emissions is different in the two cases. In the simulation using WIND data a high altitude arc is seen (Fig. 4, top panel) that is absent in the IPS data-based simulation (Fig. 4, bottom panel).

IV. COMPARISON OF THE INFLUENCE OF DIFFERENT EXOBASE TEMPERATURES

To study the temperature dependence X-ray images were calculated using neutral profiles with different exobase temperatures, using the solar wind parameters that are based on WIND measurements. Fig 5 shows five images where the the nominal exobase temperatures in table II have been scaled by a factor of 0.2; 0.5; 1; 2; and 5 respectively. The maximum X-ray radiance increases with an increasing exobase temperature, and the extent of the X-ray emitting region increases with temperature. The sharp edge in X-ray emissions that is seen on all sides, but most clearly near the bottom and along the left side, of the $T = 5T_0$ image is artificial. It appears because the image covers the whole simulation box. The

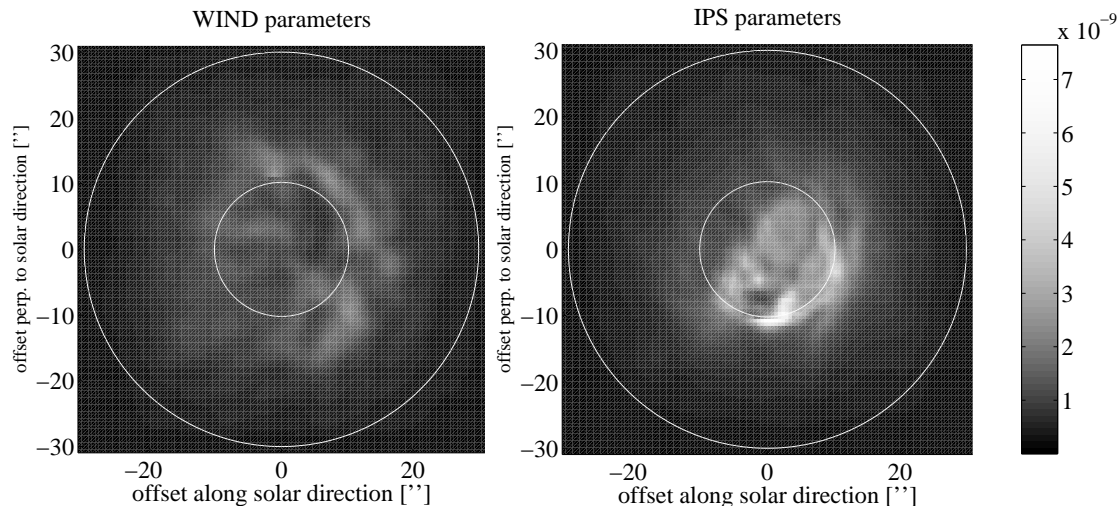


FIG. 2 Two simulated X-ray images of Mars at a phase angle of 18.2° , corresponding to the situation at the time of the observation. The phase angle is defined as the angle between the Mars-to-sun and the Mars-to-observer directions. The left panel shows the results of a simulation with input parameters estimated from data obtained by the WIND satellite using a ballistic model. The right panel shows the results of a simulation with input parameters estimated using MHD tomography based on IPS measurements. The inner white circles, with radius 10.2 arc seconds, mark the geometric size of Mars, and the outer white circles, with radius 30 arc seconds mark the extent of the X-ray halo according to Dennerl (2002). The same grey-scale is used for both images, and it shows the X-ray radiance in $\text{Wm}^{-2}\text{sr}^{-1}$.

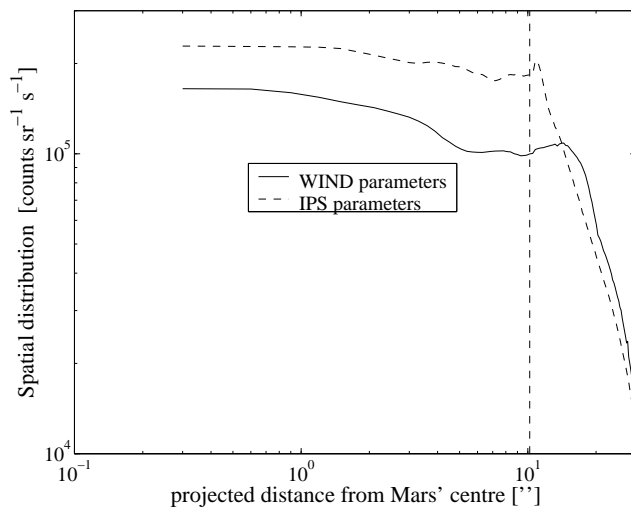


FIG. 3 Radial distribution of the simulated X-ray intensity in units of $\text{sr}^{-1}\text{s}^{-1}$. The solid curve shows the results of a simulation using input data estimated from WIND data, and the dashed curve shows the results of a simulation with input data obtained by MHD tomography of IPS measurements. The vertical dashed line marks the size of the Martian disk, which corresponds to the inner circles of the images in Fig. 2.

trajectories of the heavy ion test particles are terminated when an ion reaches the edge of the simulation box causing the heavy ion density to be lower close to the edge of the box. In addition to this finite radius effect comes a geometrical effect, because the cubical simulation box

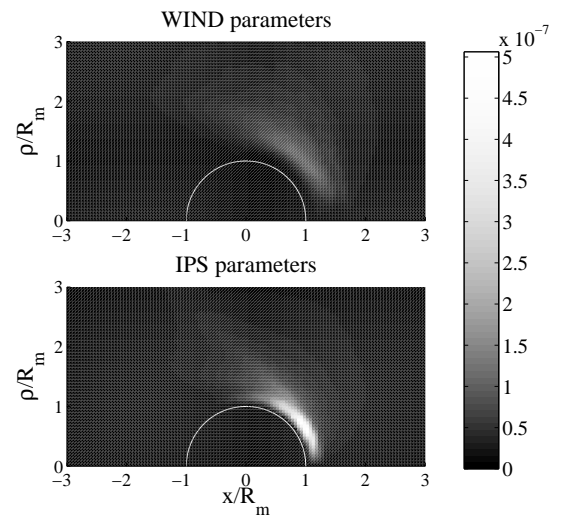


FIG. 4 X-ray emission in cylindrical coordinates for a simulation using input data estimated from WIND data (upper panel), a simulation with input data obtained by MHD tomography of IPS measurements (lower panel). The grey-scale shows the emitted X-rays in units of Wm^{-2}

is viewed from an angle of 18.2° , which makes the integration path shorter for the pixels that are located close to the vertical edges of the images than for those farther away from the edges. This computational artefact can also be seen in the $T = 2T_0$ image, if it is carefully examined. It is not seen in the first three images where, due

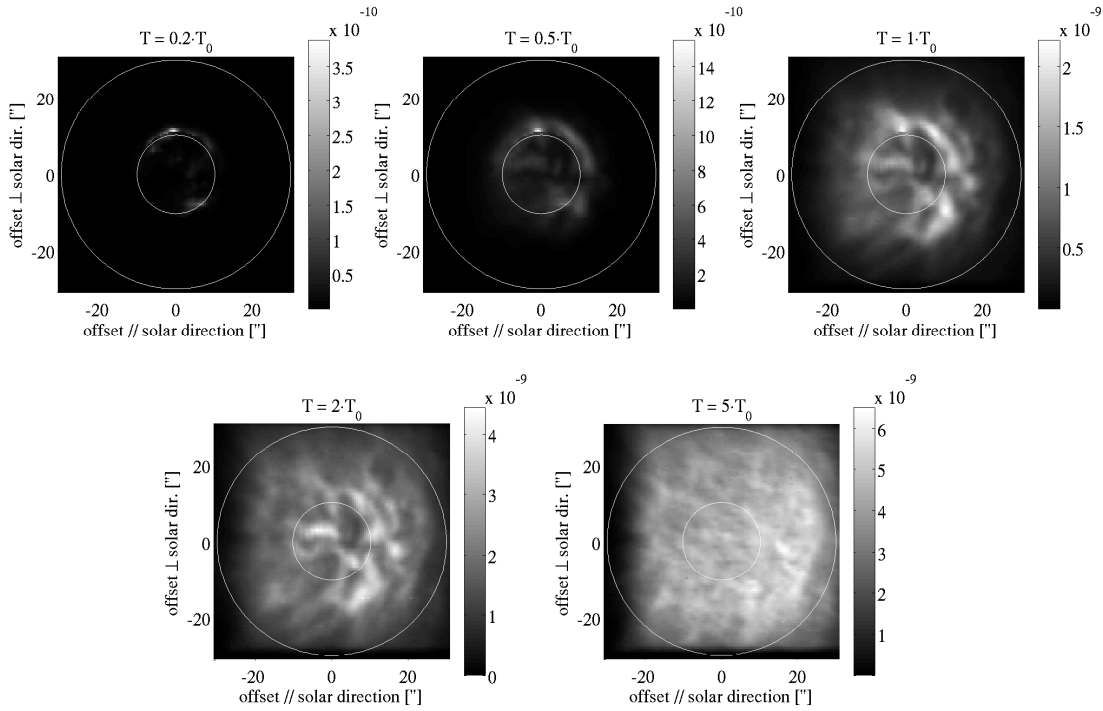


FIG. 5 Five simulated X-ray image of Mars at a phase angle of 18.2° , corresponding to the situation at the time of the observation. The phase angle is defined as the angle between the Mars-to-sun and the Mars-to-observer directions. The different panels show results obtained assuming different exobase temperatures. From top to bottom the nominal exobase temperatures in table II have been scaled by a factor of 0.2; 0.5; 1; 2; and 5 respectively. The inner white circles, with radius 10.2 arc seconds, mark the geometric size of Mars, and the outer white circles, with radius 30 arc seconds mark the extent of the X-ray halo according to Dennerl (2002). The grey-scale shows the X-ray radiance in $\text{Wm}^{-2}\text{sr}^{-1}$.

to the lower exobase temperature, there are no emissions far away from the centre of the images.

Fig. 6 shows the radial dependence of the X-ray emissions, i.e., the images in Fig. 5 have been integrated according to Eq. (7). The falloff with radial distance from the image centre is steeper for lower exobase temperatures.

When the exobase temperature increases at constant exobase density the number of neutral particles in the exosphere increases, and this yields a larger X-ray emission. The falloff of density with altitude is also steeper for lower temperatures, which is in agreement with the results for the radial dependence of the X-ray emissions in Fig. 6.

V. VARIATION OF HEAVY ION ABUNDANCES

The SWCX X-ray emissions in our model scale linearly with the heavy ion abundances. Both the abundance of one atomic species and the relative abundances of two different charge states of the same element can vary up to an order of magnitude (Zurbuchen et al., 2002). The abundances depend on the type of the solar wind, and therefore the uncertainties can be lowered considerably

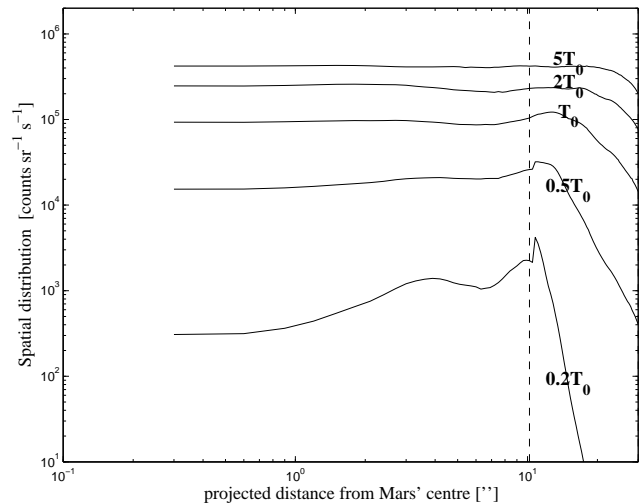


FIG. 6 Radial distribution of the simulated X-ray intensity in units of $\text{sr}^{-1}\text{s}^{-1}$. The different curves show results obtained assuming different exobase temperatures. From top to bottom the nominal exobase temperatures have been scaled by a factor of 5; 2; 1; 0.5; and 0.2 respectively. The vertical dashed line marks the size of the Martian disk, which corresponds to the inner circles of the images in Fig. 2.

with knowledge of whether the solar wind is slow or fast. This, however, requires long exposure times, since there are even larger variations on time scales on the order of minutes (Aellig et al., 1998; Wurz et al., 1998).

VI. CONCLUSIONS AND DISCUSSION

We have modelled the contribution from solar wind charge exchange to the X-ray emission at Mars. This was achieved by the use of a hybrid simulation to find the electric and magnetic fields around the planet, and then a test particle simulation was run to compute trajectories of heavy, multiply charged solar wind ions. Such simulation were used by Gunell et al. (2004) and were found to be larger than the observations made with the Chandra X-ray observatory by a factor of between 1 and 3. There are a few uncertainties involved in this simulation process.

First, the density of the neutral exosphere of Mars changes with the solar cycle, and the estimate that was used by Gunell et al. (2004) for solar maximum conditions might be incorrect for the particular time of observation. We use a Chamberlain exosphere to model the neutral exosphere densities, and the density at altitudes above the exobase is determined by the density and temperature at the exobase. Disregarding the loss of heavy ions, the X-ray emission at a particular point in space scales linearly with the neutral density at that point, and since the neutral density at any point is proportional to the density at the exobase, the X-ray emission scales linearly with exobase density. In section IV we scaled the temperature by factors of 0.2; 0.5; 1; 2; and 5 to study the temperature dependence. Since the exosphere contains a larger number of neutrals for an increased temperature the emission intensity increases with increasing temperature. The radial falloff in the X-ray halo is steeper for lower temperatures, because of the steeper falloff of the exosphere density at lower exobase temperature.

Secondly, the estimate of the solar wind parameters might be inaccurate. In section III we examined the result of hybrid simulations run with two different sets of input solar wind parameters, both obtained from measurement-based model calculations. The structure of the X-ray images thus obtained is visibly different in the two cases. The intensities of the emissions in the two cases are similar from the outer part of the halo, but differ significantly at the inner halo and the Martian disk. The emissions from lower altitude depend on how deeply the solar wind flux can penetrate into the Martian exosphere, which in turn depends on solar wind parameters such as flux and magnetic field. It is therefore important to have as accurate knowledge as possible about the solar wind parameters.

Thirdly, the composition of the solar wind, i.e. the abundances of the heavy ions, may, on the day of the observation, have differed from the estimates used. This

may significantly alter the results. The abundances change with the solar cycle and are different depending on whether the solar wind is slow or fast. Hence the intensity of the X-rays may change, and the relative importance of the different heavy ion species may be altered. The X-ray intensity is proportional to the heavy ion abundances, and is therefore directly affected by poor knowledge these. The shape and extent is only affected by the relative importance of the different ion species, and since the mass to charge ratio does not vary too much between these this is a minor effect. The uncertainties can be reduced by better knowledge of the solar wind conditions.

Fourthly, the fields obtained from the hybrid simulation may be inaccurate due to the limited spatial resolution. The hybrid model reproduces the basic plasma and magnetic field regions around Mars that were measured by the Phobos-2 mission, for example the bow shock, magnetotail, and how the magnetic field is piled up against the planet (Kallio and Janhunen, 2001, 2002).

Fifthly, there could be errors in the values that we have used for the charge exchange cross sections. The classical over-barrier cross sections that we have used are generally over-estimates, and that can contribute to the discrepancy between the measured and simulated halo emissions.

The properties of the Martian X-ray halo depend sensitively on the points discussed here, which implies that the X-ray emission contains valuable information.

VII. ACKNOWLEDGEMENT

We are grateful to Ronald P. Lepping (NASA/Goddard SFC) for the WIND MFI data, and to K.W. Ogilvie (NASA/GSFC), A.J. Lazarus (MIT), and J.C. Kasper (MIT) for the WIND SWE data. The MHD tomography IPS data were provided by the Solar-Terrestrial Environment Laboratory (STEL) of Nagoya University.

References

- Aellig, M. R., Grünwaldt, H., Bochsler, P., et al., 1998. Iron freeze-in temperatures measured by SOHO/CELIAS/CTOF. *J. Geophys. Res.* 103 (A8), 17215–17222.
- Chamberlain, J. W., Hunten, D. M., *Theory of planetary atmospheres*, 2nd Edition. Academic Press, inc., San Diego, California, 1987.
- Cravens, T. E., Comet Hyakutake x-ray source: Charge transfer and solar wind heavy ions. *Geophys. Res. Lett.* 24, 105–108, 1997.
- Cravens, T. E., X-ray emission from comets and planets. *Adv. Space Res.* 26 (10), 1443–1451, 2000.
- Cravens, T. E., X-ray emission from comets. *Science* 296, 1042–1045, 2002.

- Cravens, T. E., Maurellis, A. N., X-ray emission from scattering and fluorescence of solar x-rays at venus and mars. *Geophys. Res. Lett.* 28 (15), 3043–3046, 2001.
- Dennerl, K., Discovery of X-rays from Mars with Chandra. *Astronomy & Astrophysics* 394, 1119–1128, doi:10.1051/0004-6361:20021116, 2002.
- Dennerl, K., Burwitz, V., Englhauser, J., Lisse, C., Wolk, S. Discovery of X-rays from Venus with Chandra. *Astronomy & Astrophysics* 386, 319–330, doi:10.1051/0004-6361:20020097, 2002.
- Gunell, H., Holmström, M., Kallio, E., Janhunen, P., Dennerl, K., X-rays from solar wind charge exchange at Mars: A comparison of simulations and observations. *Geophys. Res. Lett.* 31, L22801, doi:10.1029/2004GL020953, 2004.
- Hayashi, K., Kojima, M., Tokumaru, M., Fujuki, K., MHD tomography using interplanetary scintillation measurement. *J. Geophys. Res.* 108 (A3), 1102, doi:10.1029/2002JA009567, 2003.
- Hefti, S., Grünwaldt, H., Ipavich, F. M., et al., 1998. Kinetic properties of solar wind minor ions and protons measured with SOHO/CELIAS. *J. Geophys. Res.* 103 (A12), 29697–29704.
- Hockney, R. W., Eastwood, J. W., *Computer Simulation Using Particles*. IOP Publishing Ltd, Techno House, Redcliffe Way, Bristol BS1 6NX, England, 1988.
- Holmström, M., Barabash, S., Kallio, E., X-ray imaging of the solar wind–Mars interaction. *Geophys. Res. Lett.* 28 (7), 1287–1290, 2001.
- Kallio, E., Janhunen, P., Atmospheric effects of proton precipitation in the Martian atmosphere and its connection to the Mars-solar wind interaction. *J. Geophys. Res.* 106, 5617–5634, 2001.
- Kallio, E., Janhunen, P., Ion escape from Mars in a quasi-neutral hybrid model. *J. Geophys. Res.* 107 (A3), 1035, doi:10.1029/2001JA000090, 2002.
- Kallio, E., Luhmann, J. G., Barabash, S., Charge exchange near Mars: The solar wind absorption and energetic neutral atom production. *J. Geophys. Res.* 102, 22183–22197, 1997.
- Keating, G. M., Tolson, R. H., Cancro, G. J., et al., The structure of the upper atmosphere of Mars: In situ accelerometer measurements from Mars Global Surveyor. *Science* 279 (5357), 1672–1676, 1998.
- Krasnopolsky, V., On the deuterium abundance on Mars and some related problems. *Icarus* 148, 597–602, 2000.
- Krasnopolsky, V. A., Gladstone, G. R., Helium on Mars: EUVE and PHOBOS data and implications for Mars’ evolution. *J. Geophys. Res.* 101 (A7), 15765–15772, 1996.
- Schwadron, N. A., Cravens, T. E., Implications of solar wind composition for cometary X-rays. *The Astrophysical Journal* 544, 558–566, 2000.
- Wegmann, R., Schmidt, H. U., Lisse, C. M., Dennerl, K., Englhauser, J., X-rays from comets generated by energetic solar wind particles. *Planetary and Space Science* 46 (5), 603–612, 1998.
- Wurz, P., Ipavich, F. M., Galvin A. B., et al., 1998. Elemental composition of the January 6, 1997, CME. *Geophys. Res. Lett.* 25 (14), 2557–2560.
- Zurbuchen, T. H., Fisk, L. A., Gloeckler, G., von Steiger, R., The solar wind composition throughout the solar cycle: A continuum of dynamic states. *Geophys. Res. Lett.* 29 (9), 1352, doi:10.1029/2001GL013946, 2002.